

A Patchwise Local Fourier Extension Method for Function Approximation on General Two-Dimensional Domains

Zhenyu Zhao^a, Yanfei Wang^b

^a*School of Mathematics and Statistics, Shandong University of Technology, Zibo, 255049, China*

^b*Key Laboratory of Deep Petroleum Intelligent Exploration and Development, Institute of Geology and Geophysics, Chinese Academy of Sciences, Beijing, 100029, China*

Abstract

We propose a patchwise local Fourier extension method for approximating smooth functions on general two dimensional domains with curved boundaries. The domain is embedded into a Cartesian background grid and decomposed into rectangular interior patches and one-side curved trapezoidal boundary patches. After local data transfer, all patches are converted into fixed-size tensor-product arrays and approximated by a truncated-SVD stabilized local Fourier extension procedure.

Unlike global Fourier frame approximations, the proposed method localizes both the geometry and the ill-conditioned extension process. For fixed local parameters, the local algebraic operations are performed on fixed-size systems, and the reference Fourier extension matrices and their singular value decompositions are reused across patches. Boundary patches require additional one-dimensional transfer or completion steps, but their costs remain uniformly bounded by the local resolution. Consequently, the online complexity is $O(N)$, where N denotes the total number of retained output points for fixed local resolution.

Numerical experiments on smooth curved domains and on a mildly rough boundary domain demonstrate that the method achieves high accuracy with a fixed set of local parameters. The smooth-cover correction reduces the boundary-induced error by several orders of magnitude in the full-domain rough-boundary test, without changing the underlying scan-based partition.

Keywords: Fourier extension; local approximation; function approximation on curved domains; patchwise method; curved boundary patches; TSVD regularization; scan-based partition

1. Introduction

High-order approximation of smooth functions on domains with curved boundaries is a fundamental problem in scientific computing and data science, e.g., mapping the irregular geometry of active Earth faults, mitigating boundary-induced errors at fault intersections, performing data assimilation in the local Fourier coefficient space rather than the physical grid space, and hence providing an potential spatial representation tool for complex physical modelling [1]. More broadly, it is closely related to spectral and high-order discretizations of partial differential equations, embedded

and fictitious-domain methods, inverse problems, imaging, and data processing on non-rectangular spatial regions [2–8]. On tensor-product domains, Fourier and polynomial spectral methods are known to provide highly accurate and efficient approximations. However, this advantage is much less straightforward to retain when the physical domain has a non-rectangular or curved boundary. In this case, the boundary geometry becomes a central numerical difficulty: standard tensor-product approximations do not conform naturally to the physical boundary, while unstructured or mesh-based approaches may introduce additional complications related to local approximation order, conditioning, and the accurate representation of the geometry.

A common strategy for approximating functions on non-tensor-product domains is to embed the physical domain Ω into a simple tensor-product domain D , and to restrict an approximation system on D to Ω . This leads naturally to frame approximations rather than basis approximations. In the polynomial setting, Adcock and Huybrechs studied polynomial frame approximation for smooth multivariate functions on irregular domains, using tensor-product orthogonal polynomials on a bounding box and samples taken only inside the physical domain [8]. In the Fourier setting, Fourier extension (FE), or Fourier continuation (FC), approximates nonperiodic functions by Fourier series defined on an enlarged periodic domain [2, 9, 10]. In these methods, the restricted approximation system is generally redundant and the associated discrete systems are ill-conditioned. Nevertheless, with regularization, especially truncated singular value decomposition (TSVD), stable and accurate approximations can be obtained [10–12].

For two-dimensional irregular domains, Matthysen and Huybrechs developed a global Fourier frame approximation by restricting a Fourier basis on a bounding box to samples inside the physical domain [7]. Their analysis shows that the singular values of the corresponding collocation matrix cluster near one and zero, with a relatively small transition set, or plunge region, between them. In two dimensions, the size of this plunge region is governed mainly by the boundary geometry rather than by the area of the domain. Consequently, the complexity of their fast projection algorithm is closely tied to the boundary measure and, for ordinary non-fractal planar domains, can be reduced from the cubic cost of a direct solver to $O(N^2 \log^2 N)$ [7]. This observation is important here: it suggests that, in Fourier-frame approximation on irregular domains, the main geometric difficulty is concentrated near the boundary.

Another important line of work is based on explicit continuation near the boundary. Bruno and coauthors developed high-order Fourier-continuation techniques for solving partial differential equations in general smooth domains [4–6, 13]. More recently, Bruno and Paul proposed a two-dimensional Fourier Continuation method for constructing biperiodic extensions of smooth functions on general smooth domains [14]. In such approaches, the main task is to construct smooth continuation data near the boundary so that the function can be embedded into a periodic rectangular setting and then processed efficiently by Fourier techniques such as the FFT. These methods demonstrate the effectiveness of combining Fourier approximation with careful boundary continuation, but they also show that the treatment of the boundary is a central and delicate part of Fourier-based methods on curved domains.

The discussion above suggests two complementary ways of handling irregular geometries. Global frame methods restrict a tensor-product approximation system to the physical domain and control the resulting redundancy by regularization, whereas Fourier-continuation methods construct extension data so that a periodic representation can be used

on a surrounding rectangular domain. In both cases, the geometric difficulty is strongly tied to the boundary. This motivates a local alternative: separate the relatively simple interior regions from the boundary regions, approximate each local piece by a fixed-size stabilized Fourier extension procedure, and assemble the resulting local approximations.

Localized Fourier extension strategies provide such a route. In our previous work [15], a one-dimensional local Fourier extension (LFE) method was developed for function approximation on intervals. The method partitions the target interval into subintervals and applies a stabilized Fourier extension approximation on each local piece. It retains the high accuracy of Fourier extensions for smooth functions while adapting to local variations of the target function. The local construction is also modular: once the local discretization parameters are fixed, the same reference extension matrix and its truncated singular value decomposition can be reused.

The present paper extends this LFE philosophy to two-dimensional domains with curved boundaries. The main new difficulty is geometric: a local partition must handle not only rectangular interior regions, but also curved boundary regions and transition portions where the dominant boundary direction changes. We therefore construct a patch system that is compatible with Cartesian sampling and local tensor-product Fourier extension.

The proposed method embeds the domain into a Cartesian background grid and uses a boundary scan to generate a local patch database. Interior regions are treated as rectangular patches, while boundary regions are represented by one-side curved patches of left, right, top, or bottom type. Transition regions are covered by additional one-side patches and reduced to the same four standard boundary types. On rectangular patches, tensor-product LFE is applied directly. On curved patches, boundary intersections with vertical or horizontal sampling lines are used to form a fixed-size local data array, so that the same tensor-product LFE procedure can be used. Thus the geometric information is confined to the patch construction and data transfer, while the algebraic approximation step remains uniform across all patches.

This locality gives the method a clear computational advantage. Instead of forming a single global Fourier frame system, the approximation is decomposed into local problems of fixed resolution. For rectangular patches, the tensor-product LFE procedure uses precomputed one-dimensional SVDs directly. For curved boundary patches, additional one-dimensional LFE transfers are performed along vertical or horizontal sampling lines; for mildly rough boundary patches, a one-unknown completion is also carried out on each sampling line. Since all these operations involve only a fixed number of local nodes when m, n, T and the refinement factor are fixed, the online cost is proportional to the number of patches, or equivalently $O(N)$ with respect to the number of retained output points.

The main contributions of this paper are summarized as follows.

- We develop a patchwise local Fourier extension framework for two-dimensional domains with curved boundaries. The scan-based construction reduces the domain to rectangular interior patches and four standard types of one-side curved boundary patches.
- We show how curved boundary data can be converted into fixed-size tensor-product arrays by one-dimensional local Fourier extension transfer. Consequently, all local patches are processed by the same TSVD-stabilized

tensor-product Fourier extension procedure.

- We establish a basic error estimate that relates the two-dimensional local approximation error to one-dimensional directional Fourier extension defects and to the geometry of the local patch mapping. The estimate clarifies why local subdivision reduces the effective frequency and the geometric distortion seen by each patch.
- We analyze the computational complexity of the method. For fixed local parameters, the local algebraic operations are performed on fixed-size systems with reusable SVDs, leading to $O(N)$ online complexity with respect to the total number of retained output points.
- We introduce a smooth-cover correction for boundary patches with small-scale rough perturbations. The correction constructs a local smooth cover, recovers one artificial boundary value on each sampling line using a one-dimensional Fourier extension consistency condition, and then restricts the final output to the original physical region.

Numerical experiments on both smooth and mildly rough domains demonstrate that the method achieves high accuracy with a fixed set of local parameters. The full-domain rough-boundary tests further show that the smooth-cover correction can substantially reduce boundary-induced errors without modifying the scan-based partition.

The rest of the paper is organized as follows. Section 2 formulates the patchwise local Fourier extension problem on rectangular and one-side curved patches. Section 3 gives a basic error estimate and discusses the influence of local subdivision and geometric mapping. Section 4 calibrates the main numerical parameters on rectangular patches. Section 5 describes the approximation procedure on curved trapezoidal patches, including the smooth-cover correction for mildly rough boundary patches. Section 6 presents the scan-based patch construction for general domains and analyzes the computational complexity. Section 7 reports numerical experiments, including tests on smooth curved domains and on a domain with a mildly rough boundary. Section 8 concludes the paper with several remarks on possible extensions.

2. Problem formulation

In this section, we formulate the two-dimensional patchwise local Fourier extension problem. The aim is to approximate a smooth function on a general planar domain by reducing the computation to local Fourier extension approximations on geometrically simple patches.

Let $\Omega \subset \mathbb{R}^2$ be a bounded planar domain whose boundary $\Gamma = \partial\Omega$ can be locally represented by curves. We assume that Ω is contained in a rectangular box

$$R = [x_{\min}, x_{\max}] \times [y_{\min}, y_{\max}],$$

equipped with a Cartesian background partition. The physical domain is decomposed, or covered, by a finite collection of local patches

$$\mathcal{P} = \{P_\nu\}_{\nu=1}^{N_p}.$$

The patches are either rectangular interior patches or boundary-adapted one-side curved patches. This decomposition reduces approximation on a general curved domain to a family of local approximation problems for which tensor-product Fourier extension can be used.

For an interior patch, we take

$$P_v = [x_L, x_R] \times [y_B, y_T].$$

For a boundary patch, we assume that, after choosing a suitable local coordinate direction, the patch has one curved side and three Cartesian aligned sides. Typical examples are

$$P_T = \{(x, y) : x_L \leq x \leq x_R, y_B \leq y \leq \gamma_T(x)\},$$

$$P_B = \{(x, y) : x_L \leq x \leq x_R, \gamma_B(x) \leq y \leq y_T\},$$

and, after exchanging the roles of x and y ,

$$P_L = \{(x, y) : y_B \leq y \leq y_T, \gamma_L(y) \leq x \leq x_R\},$$

$$P_R = \{(x, y) : y_B \leq y \leq y_T, x_L \leq x \leq \gamma_R(y)\}.$$

Here $\gamma_T, \gamma_B, \gamma_L, \gamma_R$ denote local representations of the boundary. Thus each boundary patch contains only one curved side. This form is convenient for constructing local tensor-product data arrays from samples along vertical or horizontal Cartesian lines.

We next introduce the local Fourier extension spaces. Let $T_x > 1$ and $T_y > 1$ be extension parameters, and set

$$\Lambda_x = \left[0, \frac{2\pi}{T_x}\right], \quad \Lambda_y = \left[0, \frac{2\pi}{T_y}\right].$$

For nonnegative integers N_x and N_y , define

$$H_{N_x}^{(x)} = \text{span}\{e^{i\ell t} : |\ell| \leq N_x\}, \quad H_{N_y}^{(y)} = \text{span}\{e^{iqs} : |q| \leq N_y\}.$$

The tensor-product local Fourier extension space is

$$H_{N_x, N_y} = H_{N_x}^{(x)} \otimes H_{N_y}^{(y)} = \text{span}\{e^{i\ell t} e^{iqs} : |\ell| \leq N_x, |q| \leq N_y\}.$$

On each patch P_v , the sampled function values are arranged into a local data matrix

$$\mathbf{F}^{(v)} \in \mathbb{C}^{m_y \times m_x}.$$

For rectangular patches, this is the usual tensor-product array in the physical coordinates. For boundary patches, the data are collected along Cartesian sampling lines and then transferred to a fixed-size tensor-product array. For example, on a top patch P_T , we use vertical sampling lines $x = x_k$, compute the boundary intersections $\gamma_T(x_k)$, and sample the function along

$$y_B \leq y \leq \gamma_T(x_k).$$

The resulting line data are converted to values on a normalized tensor grid associated with the local coordinates of the curved patch. The bottom, left, and right patch types are treated in the same way, with the appropriate choice of sampling direction.

After rescaling the local coordinates to $\Lambda_x \times \Lambda_y$, the local approximant takes the form

$$F_v(t, s) = \sum_{|\ell| \leq N_x} \sum_{|q| \leq N_y} c_{\ell, q}^{(v)} e^{i\ell t} e^{iqs}.$$

The coefficients are computed from the local data by a tensor-product least-squares procedure regularized by truncated singular value decomposition (TSVD). In practice, this is implemented by applying the one-dimensional TSVD-stabilized Fourier extension operators successively in the two coordinate directions.

The global approximation is defined patchwise. The local approximations F_v are evaluated on their corresponding physical patches and then assembled to approximate f on Ω . The construction of the patch database, the treatment of transition regions, and the practical assembly rule are described in the following sections. The basic idea is therefore to transform the approximation problem on a curved domain into a set of local Fourier extension approximations on rectangular patches and one-side curved patches.

3. A basic error estimate

In this section, we give a basic error estimate for the proposed patchwise local Fourier extension approximation. Starting from the one-dimensional TSVD-stabilized Fourier extension estimate, we show how the directional errors enter the tensor-product two-dimensional approximation and how the local map from a reference patch to a physical patch affects the final error.

3.1. One-dimensional stabilized estimate

Let

$$\mathcal{Q}_{N_x}^{\varepsilon, (x)} : L^2(\Lambda_x) \rightarrow H_{N_x}^{(x)}, \quad \mathcal{Q}_{N_y}^{\varepsilon, (y)} : L^2(\Lambda_y) \rightarrow H_{N_y}^{(y)}$$

denote the one-dimensional TSVD-stabilized Fourier extension operators in the two coordinate directions. Here $\varepsilon > 0$ is the truncation threshold. Following the one-dimensional local Fourier extension theory, we use the estimates

$$\|v - \mathcal{Q}_{N_x}^{\varepsilon, (x)} v\|_{L^2(\Lambda_x)} \leq \inf_{\mathbf{c} \in \mathbb{C}^{2N_x+1}} \left(\|v - \mathcal{F}_{N_x}^{(x)} \mathbf{c}\|_{L^2(\Lambda_x)} + \varepsilon \|\mathbf{c}\|_{\ell^2} \right), \quad v \in L^2(\Lambda_x), \quad (1)$$

and

$$\|w - \mathcal{Q}_{N_y}^{\varepsilon, (y)} w\|_{L^2(\Lambda_y)} \leq \inf_{\mathbf{d} \in \mathbb{C}^{2N_y+1}} \left(\|w - \mathcal{F}_{N_y}^{(y)} \mathbf{d}\|_{L^2(\Lambda_y)} + \varepsilon \|\mathbf{d}\|_{\ell^2} \right), \quad w \in L^2(\Lambda_y). \quad (2)$$

These estimates state that the stabilized one-dimensional reconstruction is controlled by the best Fourier extension approximation error together with the TSVD regularization term.

3.2. Local estimate on a reference patch

Let

$$\Lambda = \Lambda_x \times \Lambda_y.$$

For $g \in L^2(\Lambda)$, define the tensor-product local Fourier extension operator

$$\mathcal{Q}_{N_x, N_y}^\varepsilon = \mathcal{Q}_{N_x}^{\varepsilon, (x)} \otimes \mathcal{Q}_{N_y}^{\varepsilon, (y)}.$$

This corresponds to applying the one-dimensional stabilized reconstructions successively in the two coordinate directions.

For later use, define the directional reconstruction errors

$$\mathcal{E}_x(g) = \left(\int_{\Lambda_y} \|g(\cdot, s) - \mathcal{Q}_{N_x}^{\varepsilon, (x)} g(\cdot, s)\|_{L^2(\Lambda_x)}^2 ds \right)^{1/2},$$

and

$$\mathcal{E}_y(g) = \left(\int_{\Lambda_x} \|g(t, \cdot) - \mathcal{Q}_{N_y}^{\varepsilon, (y)} g(t, \cdot)\|_{L^2(\Lambda_y)}^2 dt \right)^{1/2}.$$

Lemma 3.1. *Assume that the stabilized one-dimensional reconstruction in the x -direction is bounded on $L^2(\Lambda_x)$, namely*

$$\|\mathcal{Q}_{N_x}^{\varepsilon, (x)}\|_{L^2(\Lambda_x) \rightarrow L^2(\Lambda_x)} \leq \kappa_x.$$

Then

$$\|g - \mathcal{Q}_{N_x, N_y}^\varepsilon g\|_{L^2(\Lambda)} \leq \mathcal{E}_x(g) + \kappa_x \mathcal{E}_y(g). \quad (3)$$

Proof. Using the identity

$$I - \mathcal{Q}_{N_x, N_y}^\varepsilon = (I - \mathcal{Q}_{N_x}^{\varepsilon, (x)}) \otimes I + \mathcal{Q}_{N_x}^{\varepsilon, (x)} \otimes (I - \mathcal{Q}_{N_y}^{\varepsilon, (y)}),$$

we apply the triangle inequality. The first term gives $\mathcal{E}_x(g)$ by Fubini's theorem, while the second term is bounded by $\kappa_x \mathcal{E}_y(g)$. This proves (3). \square

Combining Lemma 3.1 with (1)–(2), the two-dimensional reference-patch error can be controlled by the one-dimensional Fourier extension approximation defects in the two coordinate directions. Define

$$\mathcal{D}_x(g) = \left(\int_{\Lambda_y} \inf_{\mathbf{c}(s)} \left(\|g(\cdot, s) - \mathcal{F}_{N_x}^{(x)} \mathbf{c}(s)\|_{L^2(\Lambda_x)} + \varepsilon \|\mathbf{c}(s)\|_{\ell^2} \right)^2 ds \right)^{1/2},$$

and

$$\mathcal{D}_y(g) = \left(\int_{\Lambda_x} \inf_{\mathbf{d}(t)} \left(\|g(t, \cdot) - \mathcal{F}_{N_y}^{(y)} \mathbf{d}(t)\|_{L^2(\Lambda_y)} + \varepsilon \|\mathbf{d}(t)\|_{\ell^2} \right)^2 dt \right)^{1/2}.$$

Then

$$\|g - \mathcal{Q}_{N_x, N_y}^\varepsilon g\|_{L^2(\Lambda)} \leq \mathcal{D}_x(g) + \kappa_x \mathcal{D}_y(g). \quad (4)$$

Remark 3.2 (Local subdivision and effective frequency). *The quantities $\mathcal{D}_x(g)$ and $\mathcal{D}_y(g)$ measure the one-dimensional Fourier extension approximation defects of the pulled-back function g in the two coordinate directions. If g is smooth and has moderate local oscillation, then the residual terms in these quantities are small for suitable coefficient vectors $\mathbf{c}(s)$ and $\mathbf{d}(t)$ with moderate ℓ^2 -norms.*

The role of the patch partition is analogous to that in the one-dimensional local Fourier extension method. If the physical function contains an oscillatory component of frequency ω_x in the x -direction, then on a patch of width Δx its effective local frequency after rescaling is proportional to $\omega_x \Delta x$. Therefore, refining the partition reduces the local frequency seen by the Fourier extension approximation. This explains why fixed moderate Fourier orders can remain effective on sufficiently small patches.

3.3. Patchwise estimate on the physical domain

Let P be a local physical patch, either rectangular or one-side curved, and let

$$\Psi_P : \widehat{Q} \rightarrow P$$

be the corresponding map from a fixed reference square \widehat{Q} . After an affine rescaling from \widehat{Q} to $\Lambda = \Lambda_x \times \Lambda_y$, we still denote the pulled-back function by

$$g_P = f \circ \Psi_P.$$

Assume that Ψ_P is bi-Lipschitz and that

$$0 < J_{P,\min} \leq |\det D\Psi_P| \leq J_{P,\max} < \infty.$$

Let

$$G_P = \mathcal{Q}_{N_x, N_y}^{\varepsilon} g_P$$

be the local Fourier extension approximation on the reference patch, and define

$$F_P(x, y) = G_P(\Psi_P^{-1}(x, y)), \quad (x, y) \in P.$$

Theorem 3.3. *Under the assumptions above,*

$$\|f - F_P\|_{L^2(P)} \leq J_{P,\max}^{1/2} \left(\mathcal{E}_x(g_P) + \kappa_x \mathcal{E}_y(g_P) \right). \quad (5)$$

Equivalently, in terms of the directional best-approximation defects,

$$\|f - F_P\|_{L^2(P)} \leq J_{P,\max}^{1/2} \left(\mathcal{D}_x(g_P) + \kappa_x \mathcal{D}_y(g_P) \right). \quad (6)$$

Proof. By the change of variables $(x, y) = \Psi_P(\xi, \eta)$, we have

$$\|f - F_P\|_{L^2(P)}^2 = \int_{\widehat{Q}} |g_P(\xi, \eta) - G_P(\xi, \eta)|^2 |\det D\Psi_P(\xi, \eta)| d\xi d\eta.$$

Using the upper bound on the Jacobian determinant gives

$$\|f - F_P\|_{L^2(P)} \leq J_{P,\max}^{1/2} \|g_P - G_P\|_{L^2(\widehat{Q})}.$$

After accounting for the affine rescaling between \widehat{Q} and Λ , Lemma 3.1 yields (5). Estimate (6) follows from (4). \square

3.4. Global patchwise estimate

Assume that the final physical output is assigned on a collection of patches \mathcal{P} . If the output patches have disjoint interiors, then

$$\|f - F\|_{L^2(\Omega)}^2 = \sum_{P \in \mathcal{P}} \|f - F_P\|_{L^2(P)}^2.$$

Therefore, by Theorem 3.3,

$$\|f - F\|_{L^2(\Omega)} \leq \left(\sum_{P \in \mathcal{P}} J_{P,\max} (\mathcal{E}_x(g_P) + \kappa_x \mathcal{E}_y(g_P))^2 \right)^{1/2}. \quad (7)$$

Using the directional best-approximation form, we also obtain

$$\|f - F\|_{L^2(\Omega)} \leq \left(\sum_{P \in \mathcal{P}} J_{P,\max} (\mathcal{D}_x(g_P) + \kappa_x \mathcal{D}_y(g_P))^2 \right)^{1/2}. \quad (8)$$

If several local approximations are available at the same physical point, the final approximation is defined by a fixed patchwise assembly rule. Such a rule specifies which local approximation contributes to the global output and does not change the local form of the estimate.

Remark 3.4 (Effect of boundary patch size). *The Jacobian factor and the smoothness of the pulled-back function are the two places where the geometry of a curved boundary patch enters the estimate. For example, consider a top-type patch*

$$P_T = \{(x, y) : a \leq x \leq b, y_B \leq y \leq \gamma(x)\},$$

and set

$$\Delta x = b - a, \quad H(x) = \gamma(x) - y_B.$$

The standard map

$$x = a + \Delta x \xi, \quad y = y_B + \eta H(a + \Delta x \xi), \quad (\xi, \eta) \in [0, 1]^2,$$

has

$$\det D\Psi = \Delta x H(a + \Delta x \xi).$$

Thus the determinant is controlled by the local width and height of the patch. More importantly, after normalizing the patch to a fixed reference rectangle with a representative height H_0 , the curved boundary becomes

$$\widehat{\gamma}(\xi) = \frac{\gamma(a + \Delta x \xi) - y_B}{H_0}.$$

Its second derivative satisfies

$$\widehat{\gamma}''(\xi) = \frac{(\Delta x)^2}{H_0} \gamma''(a + \Delta x \xi).$$

If the boundary patches have bounded aspect ratio, so that $H_0 \asymp \Delta x$, then

$$\|\widehat{\gamma}''\|_{L^\infty(0,1)} \leq C \Delta x \|\gamma''\|_{L^\infty(a,b)}.$$

Therefore, although the physical curvature of the boundary is unchanged, the normalized curved side on each reference patch becomes closer to a straight segment as the partition is refined. This reduces the non-affine geometric distortion of the pulled-back function and helps decrease the error constants associated with boundary patches.

4. Parameter calibration on rectangular patches

Before treating curved and general-domain patches, we first calibrate the main local parameters of the tensor-product Fourier extension operator on rectangular patches. Rectangular patches do not involve geometric distortion, and therefore provide a clean setting for testing the approximation behavior of the local algebraic procedure itself. In the x -direction the relevant parameters are the extension parameter T_x , the sampling ratio γ_x , and the local Fourier order N_x , with analogous parameters in the y -direction.

In the parameter tests, we use the separable oscillatory function

$$F(x, y) = \exp(i\omega_x x) \exp(i\omega_y y),$$

where ω_x and ω_y denote the physical frequencies in the x - and y -directions, respectively. Since the present calibration is intended to identify the effective selection rule for the x -direction parameters, the figures mainly report the dependence of the error on T_x , N_x , γ_x , and ω_x . We also tested the influence of the y -direction parameters on the x -direction calibration, but the observed effect was minor and did not change the admissible ranges or the threshold behavior reported below. For this reason, only the representative x -direction tests are displayed.

The numerical tests show that the tensor-product construction inherits the essential parameter-selection mechanism of the one-dimensional local Fourier extension method. For fixed local frequency and Fourier order, there is an admissible range

$$T_{x,\min} \leq T_x \leq T_{x,\max}$$

in which the approximation reaches the accuracy level determined by the TSVD threshold and double precision. The lower bound $T_{x,\min}$ is mainly controlled by the sampling ratio γ_x , while the upper admissible range is affected by the local oscillation level ω_x and the Fourier order N_x . Once T_x lies in the admissible range, the error decreases rapidly as N_x passes a threshold value. The additional cross tests with respect to the y -direction parameters indicate that this x -direction selection rule is only weakly affected by variations in the transverse direction.

Figure 1 summarizes representative tests. The first row shows how the error depends on the extension parameter T_x , while the second row shows its dependence on the Fourier order N_x . The results confirm that T_x , γ_x , and N_x should be selected jointly.

To quantify the effect of oversampling, Table 1 lists the observed lower admissible bounds $T_{x,\min}$ for several choices of γ_x . As in the one-dimensional local Fourier extension method, increasing γ_x decreases the lower threshold of the admissible range. In particular, the choice $T = 4$ is not admissible for $\gamma = 1$, but becomes admissible when the sampling ratio is mildly increased to $\gamma = 1.2$.

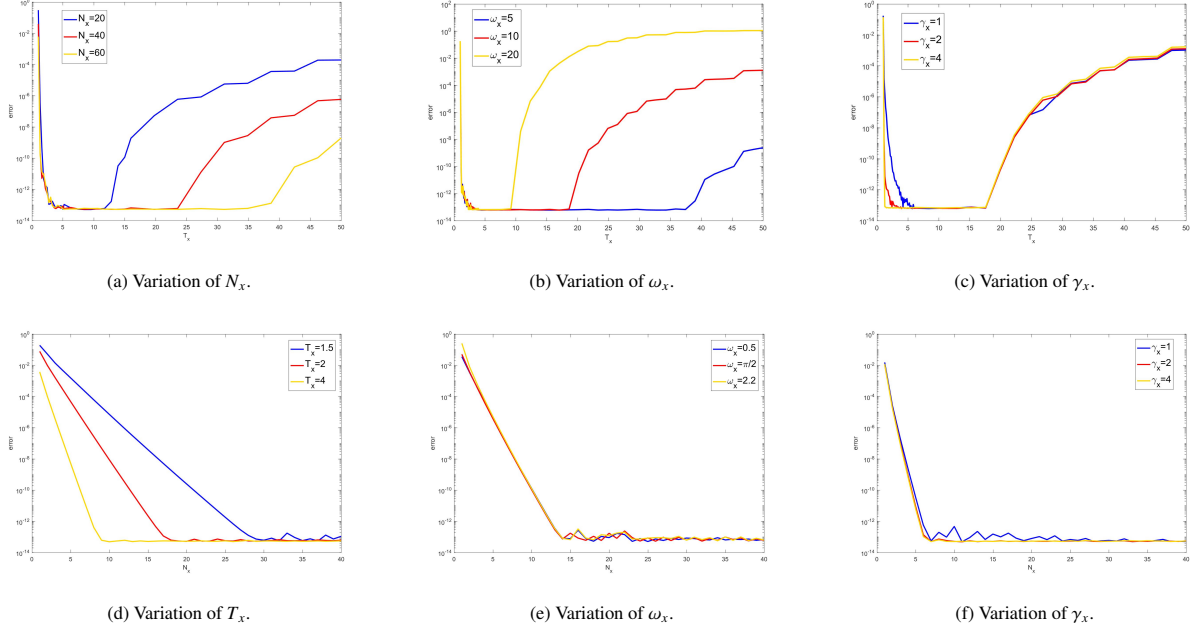


Figure 1: Representative parameter tests on rectangular patches for the separable oscillatory function $F(x, y) = \exp(i\omega_x x) \exp(i\omega_y y)$. The first row shows the dependence of the error on the extension parameter T_x , and the second row shows the dependence on the local Fourier order N_x .

Table 1: Observed lower admissible bound $T_{x,\min}$ for several oversampling ratios γ_x on rectangular patches.

	$\gamma = 1$	$\gamma = 1.2$	$\gamma = 1.5$	$\gamma = 2$	$\gamma = 4$
$T_{x,\min}$	5.5	3.9	2.9	2.2	1.2

Table 2: Observed threshold values of the local Fourier order N_x required to reach the target accuracy for different extension parameters T_x .

	$T_x = 1.2$	$T_x = 1.5$	$T_x = 2$	$T_x = 3$	$T_x = 4$	$T_x = 6$
N_x	58	27	17	13	10	9

The second relation concerns the local Fourier order N_x . Once T_x is admissible, the numerical error drops rapidly when N_x exceeds a threshold value. Table 2 records the observed thresholds for several choices of T_x . Very small extension parameters require much larger Fourier orders: for example, $T_x = 1.2$ requires $N_x = 58$, whereas $T_x = 4$ requires only $N_x = 10$, and $T_x = 6$ requires $N_x = 9$. Thus increasing T_x can reduce the required Fourier order, but this benefit must be balanced against local resolution.

The reason for not simply taking T_x as large as possible is local resolution. Suppose that the target function contains an x -direction oscillatory component with physical frequency ω_x . On a patch of width Δx , after rescaling to the Fourier extension interval $[0, 2\pi/T_x]$, the effective local frequency is proportional to

$$\mu_x = \frac{\omega_x \Delta x T_x}{2\pi}.$$

For a local Fourier space with modes $|\ell| \leq N_x$, a practical resolution condition is

$$\mu_x \lesssim N_x.$$

Thus, for fixed N_x and patch size, a smaller admissible value of T_x improves the ability of the local approximation to resolve oscillations. Equivalently, for a fixed oscillatory function, reducing T_x can reduce the required number of subintervals. Therefore, although $T = 6$ slightly reduces the Fourier order required to reach the target accuracy compared with $T = 4$, it also weakens the local resolution capability.

The parameter choice should also account for the cost of the local operations. In one coordinate direction, the number of local sampling points satisfies

$$m_x \approx \gamma_x(2N_x + 1).$$

Larger γ_x or N_x increases the size of the local matrices and the number of retained singular components in the TSVD procedure. Since the reference matrices are precomputed and reused, this cost remains local; but an efficient parameter choice should keep the local sampling size and the number of retained modes moderate. The global complexity of the full patchwise method will be discussed in Section 6.

The robust one-dimensional parameter set

$$T = 6, \quad \gamma = 1, \quad N = 9$$

is stable and effective. The present rectangular-patch tests indicate that a slightly smaller extension parameter, together with mild oversampling, provides a better balance for the two-dimensional patchwise computations. Specifically, reducing T from 6 to 4 improves local resolution, while Table 1 shows that increasing the sampling ratio from $\gamma = 1$ to $\gamma = 1.2$ is sufficient to keep $T = 4$ inside the admissible range. Table 2 further shows that the corresponding Fourier order $N = 10$ is sufficient to reach the target accuracy and remains close to the value $N = 9$ used with $T = 6$.

Based on these observations, we adopt

$$T_x = T_y = 4, \quad \gamma_x = \gamma_y = 1.2, \quad N_x = N_y = 10$$

as the default local parameter set in the numerical experiments. This choice keeps the extension parameter small enough to retain local resolution, while maintaining stability through mild oversampling. The local Fourier order is moderate, so the corresponding local matrices remain small and can be reused efficiently.

These values should be understood as practical reference choices for double-precision computations with a TSVD threshold close to machine precision. If higher-precision arithmetic or a different truncation threshold is used, the admissible range of T , the number of retained singular components, and the recommended values of N and γ should be recalibrated.

5. Approximation on curved trapezoidal patches

In this section, we describe the treatment of one-side curved trapezoidal patches. These patches are the basic boundary components used later in the scan-based construction of general domains. We first present the standard LFE-based transfer for a smooth curved side, then show why local subdivision improves the accuracy, and finally introduce a smooth-cover correction for boundary patches with small-scale rough perturbations.

5.1. Sampling nodes and LFE-based vertical transfer

It is sufficient to describe the procedure for a representative top-type curved trapezoidal patch

$$\Omega_b = \{(x, y) : x \in [a, b], 0 \leq y \leq b(x)\},$$

where $b(x) > 0$ describes the curved upper boundary. Bottom, left, and right patches are treated analogously, by reversing the normal direction or exchanging the roles of x and y .

For the top patch, we use an x -aligned semi-structured sampling strategy. The nodes in the x -direction are equispaced,

$$x_i = a + i\Delta x, \quad i = 0, 1, \dots, m_x - 1.$$

For each fixed x_i , the physical sampling nodes lie on the vertical segment

$$\{(x_i, y) : 0 \leq y \leq b(x_i)\}.$$

In the implementation, the boundary point $y = b(x_i)$ is included so that the curved side is explicitly incorporated into the sampled data. Figure 2 illustrates this sampling pattern. The blue circles denote the physical sampling nodes on the curved trapezoidal patch, while the red dots indicate the mapped target nodes after the vertical transfer. For graphical clarity, only a reduced number of nodes is displayed; the actual computations use the same sampling strategy with the prescribed local resolution.

To convert the data on the curved patch into a rectangular tensor-product array, we introduce target nodes on each vertical line,

$$y_{i,j}^* = \frac{j}{m_y - 1} b(x_i), \quad j = 0, 1, \dots, m_y - 1.$$

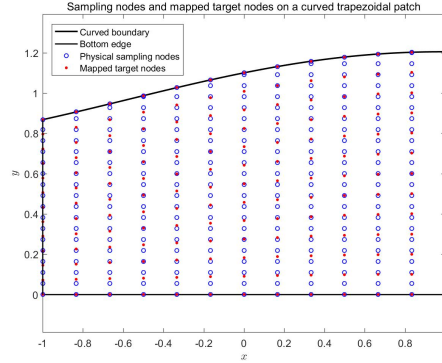


Figure 2: Sampling and vertical-transfer nodes on a representative top-type curved trapezoidal patch.

These nodes correspond to an equispaced discretization in the normalized vertical coordinate

$$\eta = \frac{y}{b(x)} \in [0, 1].$$

The values at the target nodes are obtained by applying the one-dimensional local Fourier extension procedure along each vertical line. In this way, the data on the curved trapezoid are transferred to a fixed-size rectangular array without using low-order interpolation.

After the vertical LFE transfer, we obtain

$$F_{j,i} \approx u\left(x_i, \frac{j}{m_y - 1} b(x_i)\right), \quad i = 0, \dots, m_x - 1, \quad j = 0, \dots, m_y - 1.$$

This array is then processed by the tensor-product local Fourier extension procedure for rectangular patches. Thus, the standard treatment of a curved trapezoidal patch consists of two local stages: a one-dimensional LFE-based line transfer followed by a tensor-product LFE approximation on the resulting rectangular data.

5.2. Effect of vertical subdivision on curved trapezoidal patches

We next examine the influence of the curved boundary geometry on the approximation accuracy. The purpose is to show that, when the curved side has a relatively large variation on a single patch, further local subdivision can reduce the geometric distortion and improve the approximation.

We consider

$$b(x) = 1 + 0.5x^2 + 0.2 \cos(\pi x + 0.30), \quad -1 \leq x \leq 1,$$

and the corresponding patch

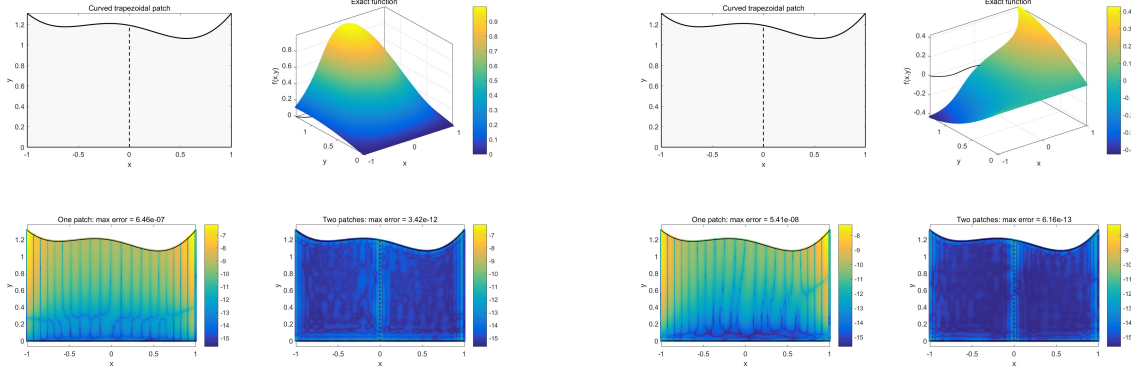
$$\Omega_b = \{(x, y) : -1 \leq x \leq 1, 0 \leq y \leq b(x)\}.$$

Although $b(x)$ is smooth, its height variation is sufficient to reveal the effect of using a single large curved patch. We compare the following two treatments:

- one-patch treatment: Ω_b is approximated as one curved trapezoidal patch,
- two-patch treatment: Ω_b is divided vertically at $x = 0$ into two curved trapezoidal patches.

The two test functions are

$$u_1(x, y) = \frac{\sin(xy/2)}{1 + y^2/4}, \quad u_2(x, y) = \cos(1.45x) \sin(1.37y).$$



(a) $u_1(x, y) = \sin(xy/2)/(1+y^2/4)$. The maximum error is reduced from 6.46×10^{-7} to 3.42×10^{-12} . (b) $u_2(x, y) = \cos(1.45x) \sin(1.37y)$. The maximum error is reduced from 5.41×10^{-8} to 6.16×10^{-13} .

Figure 3: Effect of vertical subdivision on a curved trapezoidal patch. Splitting the patch reduces the geometric distortion and significantly improves the approximation accuracy.

Figure 3 shows the results. For u_1 , the one-patch treatment gives a maximum error of about 6.46×10^{-7} , whereas the two-patch treatment reduces the maximum error to about 3.42×10^{-12} . For u_2 , the maximum error is reduced from about 5.41×10^{-8} to about 6.16×10^{-13} . Thus, in both cases, splitting the curved trapezoidal patch into two smaller patches leads to a substantial improvement, with the post-splitting errors approaching the level of machine precision.

This observation is consistent with the geometric discussion in Section 3. A curved boundary patch is mapped to a reference rectangle before the tensor-product LFE procedure is applied. If a patch contains a relatively long curved side, the normalized boundary may have a larger non-affine component, which can amplify the local approximation error. After subdivision, each subpatch contains a shorter portion of the curved boundary; the normalized curve is closer to a straight segment, and the geometric contribution to the error constant is reduced.

5.3. Smooth-cover correction for mildly rough boundary patches

The preceding construction assumes that the curved side can be used directly as a local boundary graph. We now describe a local correction for boundary patches whose curved side contains small-scale rough perturbations. The correction does not change the scan-based patch classification; it only modifies the solver used for the affected boundary patches.

For clarity, we describe the procedure for a top-type patch

$$P = \{(x, y) : x_L \leq x \leq x_R, y_B \leq y \leq b(x)\},$$

where $b(x)$ is the original rough boundary segment. Bottom patches are handled by reversing the normal direction, and left or right patches are handled by exchanging the roles of x and y .

Since the boundary has already been localized by the patch partition, we assume that the height variation of $b(x)$ on $[x_L, x_R]$ is moderate. Let $p_d(x)$ be a low-degree polynomial fit, with $d = 3$ in the numerical experiments, to boundary samples on this interval. We define a smooth cover

$$b_c(x) = p_d(x) + \delta, \quad \delta = \max_i \{b(x_i) - p_d(x_i)\} + \delta_0,$$

where $\{x_i\}$ are sufficiently dense boundary samples and $\delta_0 > 0$ is a small safety margin. Then $b_c(x)$ stays above the sampled rough boundary. The computation is performed on the smooth covering patch

$$P_c = \{(x, y) : x_L \leq x \leq x_R, y_B \leq y \leq b_c(x)\},$$

but the final output is retained only in the original physical patch P .

The values on the artificial boundary $y = b_c(x)$ are not assumed to be known. They are recovered column by column from the available data inside P . For a fixed vertical line $x = x_k$, let

$$y_{k,1}, \dots, y_{k,m_k}$$

be the available nodes in the original region, consisting of the uniform background-grid nodes below the rough boundary together with the boundary intersection $b(x_k)$. We add one artificial node at

$$y_{k,m_k+1} = b_c(x_k).$$

The corresponding data vector is

$$\mathbf{f}_k = (f(x_k, y_{k,1}), \dots, f(x_k, y_{k,m_k}), \alpha_k)^T,$$

where $\alpha_k \approx f(x_k, b_c(x_k))$ is the only unknown.

Since the nodes $y_{k,1}, \dots, y_{k,m_k}, b_c(x_k)$ are generally nonuniform, a one-dimensional Fourier extension matrix A_k is constructed separately for this column. Let

$$A_k = U_k \Sigma_k V_k^*$$

be its singular value decomposition, and let $U_{k,0}$ contain the left singular vectors corresponding to singular values below the truncation threshold. A stable Fourier extension data vector should have a small component in these discarded left-singular directions. Therefore the artificial value is determined from the consistency condition

$$U_{k,0}^* \mathbf{f}_k \approx 0.$$

Writing

$$U_{k,0} = \begin{pmatrix} U_{k,0}^{\text{in}} \\ u_{k,0}^{\text{out}} \end{pmatrix},$$

where the last row corresponds to the artificial cover node, we compute

$$\alpha_k = \arg \min_{\alpha} \left\| (U_{k,0}^{\text{in}})^* \mathbf{f}_k^{\text{in}} + \overline{u_{k,0}^{\text{out}}} \alpha \right\|_2.$$

Only one unknown is recovered on each sampling line. After this completion, the column data are projected onto the stable Fourier extension space and evaluated on the usual m -point target grid associated with P_c . The completed data are then processed by the standard top-type curved-patch solver from Section 5.1, and the final values used in the global approximation are restricted to P . Thus the rough boundary is used to determine the physical output region, while the smooth cover is used only to provide a stable local computational patch.

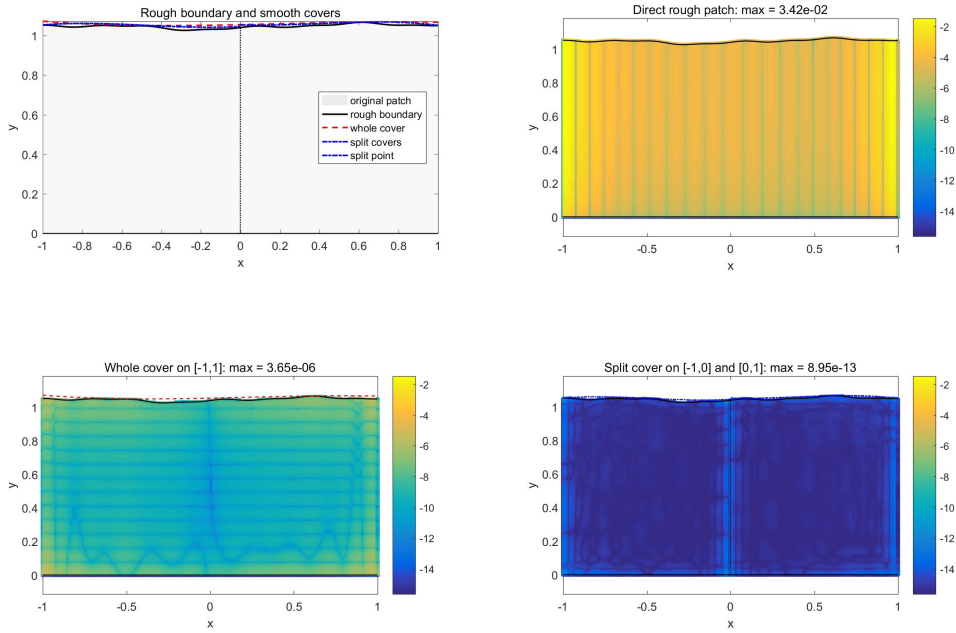


Figure 4: Patch-level test of the smooth-cover correction on a mildly rough top boundary. The three error plots correspond to direct treatment, one global smooth cover, and two local smooth covers after subdivision.

To verify the local correction mechanism, we consider a mildly rough top-type patch

$$P = \{(x, y) : -1 \leq x \leq 1, 0 \leq y \leq b(x)\}.$$

Figure 4 compares three treatments: direct use of the rough boundary, one smooth cover on the whole interval $[-1, 1]$, and two local smooth covers recomputed on $[-1, 0]$ and $[0, 1]$. The maximum error is reduced from 3.42×10^{-2} to 3.65×10^{-6} , and further to 8.95×10^{-13} after local subdivision.

This patch-level test is consistent with the subdivision effect observed in Section 5.2. In both the smooth and mildly rough cases, local subdivision reduces the difficulty of the boundary patch: it decreases the geometric distortion for

smooth curved sides and produces closer smooth covers for rough boundary portions. This provides an additional verification of the local patchwise principle underlying the proposed method.

6. Patch construction for general domains and complexity analysis

6.1. Scan-based partition into local patches

We now describe how a general two-dimensional domain is decomposed into local patches suitable for the tensor-product Fourier extension procedure. The basic idea is to embed the domain into a Cartesian background grid, scan the boundary curve once, and use the scanning result to construct rectangular interior patches and one-side curved boundary patches.

Let $\Omega \subset \mathbb{R}^2$ be a bounded domain enclosed by a closed curve

$$\Gamma = \{(x(t), y(t)) : 0 \leq t < 2\pi\}.$$

Assume that

$$\Omega \subset [a, b] \times [c, d],$$

and introduce a Cartesian partition

$$a = x_0 < x_1 < \cdots < x_{K_x} = b, \quad c = y_0 < y_1 < \cdots < y_{K_y} = d.$$

The corresponding background cells are denoted by

$$Q_{ij} = [x_{i-1}, x_i] \times [y_{j-1}, y_j], \quad 1 \leq i \leq K_x, \quad 1 \leq j \leq K_y.$$

The boundary is scanned in a fixed orientation after computing its intersections with the Cartesian grid lines. During this scan, each boundary arc is assigned one of four local directional types

$$L, \quad T, \quad R, \quad B,$$

according to whether the boundary portion is locally represented as the left, top, right, or bottom side of a computational patch. This classification is local: the same directional type may appear in several separated portions of a general boundary, and transitions between different types may occur more than once.

Interior cells are treated as rectangular patches and are labeled as *rect*. Exterior regions are discarded. Boundary arcs generate one-side curved trapezoidal patches. The four typical forms are

$$\Omega_L = \{(x, y) : y_B \leq y \leq y_T, \gamma_L(y) \leq x \leq x_R\},$$

$$\Omega_R = \{(x, y) : y_B \leq y \leq y_T, x_L \leq x \leq \gamma_R(y)\},$$

$$\Omega_T = \{(x, y) : x_L \leq x \leq x_R, y_B \leq y \leq \gamma_T(x)\},$$

$$\Omega_B = \{(x, y) : x_L \leq x \leq x_R, \gamma_B(x) \leq y \leq y_T\}.$$

Here $\gamma_L, \gamma_R, \gamma_T, \gamma_B$ are local representations of the boundary curve. Each boundary patch has one curved side inherited from Γ and three straight sides aligned with the Cartesian grid. This form is convenient for the subsequent computation, since the patch can be sampled along vertical or horizontal lines and converted to a tensor-product data array.

Near transition portions of the boundary, additional covering patches are introduced. These corner covers are not new approximation types; each of them is converted into one of the four standard types $L, T, R,$ or B , according to the local sampling direction. Thus all boundary regions are eventually handled by the same four curved-patch solvers.

Figure 5 illustrates the scan-based construction for a smooth curved boundary. The left panel shows the boundary scan and the local directional labels. The right panel shows the corresponding patch classification: interior rectangles are labeled as *rect*, exterior regions are shown as the gray background, and boundary patches are displayed as one-side curved trapezoidal patches. The red outlines indicate the additional cover patches used near transition regions.

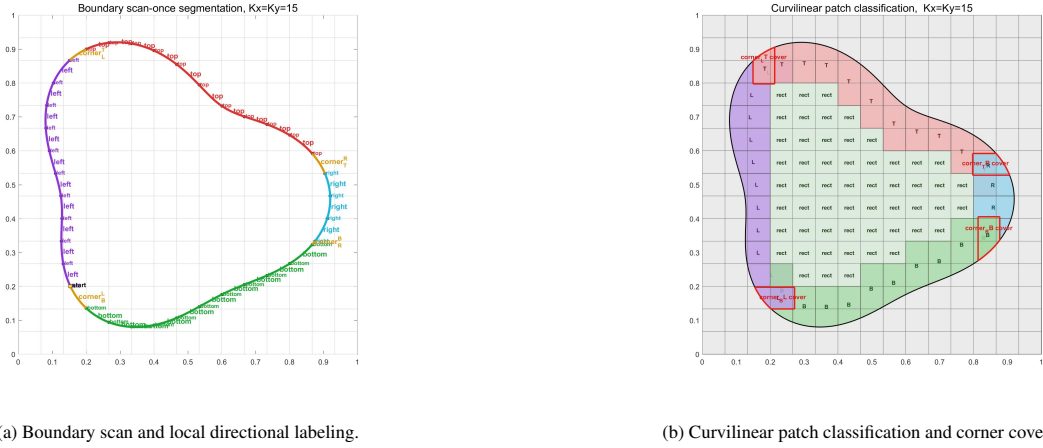


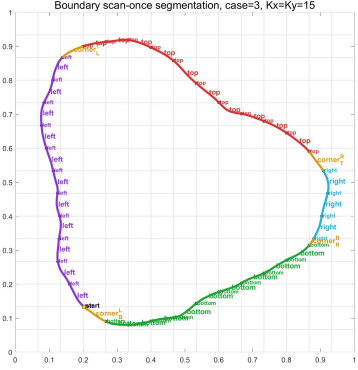
Figure 5: Scan-based patch construction for a smooth curved boundary.

The same scan-based construction can also be applied to a boundary with small-scale local perturbations. Figure 6 shows a representative example. Although the boundary contains visible local oscillations, the scan still produces the same types of local objects: rectangular interior patches, one-side boundary patches of type L, T, R, B , and corner covers. Therefore the roughness does not require a new partition logic. It is handled at the boundary-patch solver level by the smooth-cover correction described in Section 5.3.

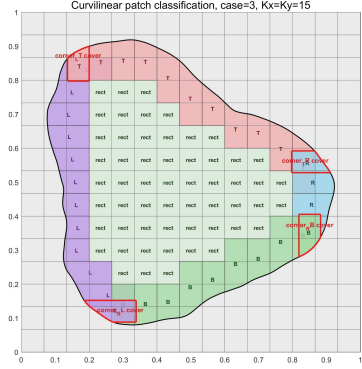
6.2. Computational complexity

We briefly summarize the computational complexity of the proposed patchwise local Fourier extension method. The detailed constructions on rectangular patches, curved trapezoidal patches, and mildly rough boundary patches have been described in the preceding sections. Here we emphasize the overall scaling of the algorithm.

Let $q = 2N + 1$ be the number of one-dimensional Fourier modes, m the number of local sampling points in each



(a) Boundary scan and directional labeling for a boundary with small-scale perturbations.



(b) Patch classification and corner covers for the perturbed boundary.

Figure 6: Scan-based patch construction for a mildly rough boundary obtained by a small radial perturbation of a smooth reference curve. The same classification mechanism is used as in the smooth case: interior rectangular patches, one-side boundary patches, and corner covers are generated from the boundary scan.

coordinate direction, and

$$I = \#\{j : \sigma_j > \varepsilon\}$$

the number of retained singular values in the TSVD procedure. For fixed parameters m, N, T and a fixed refinement factor, these quantities are moderate constants independent of the number of patches.

The offline part consists of constructing the reference one-dimensional Fourier extension matrix and computing its truncated singular value decomposition. Since the reference matrix has size $m \times q$, this cost is $O(mq^2 + q^3)$, and is paid only once for a fixed set of local parameters. The same singular systems are reused throughout the computation whenever the corresponding local discretization is the same.

The geometric preprocessing includes the scan of the boundary curve, the classification of local boundary directions, and the construction of the patch database. If N_Γ denotes the number of discrete boundary points and K_x, K_y are the numbers of background grid intervals, a direct implementation costs $O(N_\Gamma(K_x + K_y) + K_x K_y)$. This step is also performed only once for a fixed domain.

After preprocessing, the online approximation is local. Each interior rectangular patch is handled by the tensor-product local Fourier extension procedure. Each curved boundary patch is first converted to an $m \times m$ structured data array by one-dimensional LFE transfer along vertical or horizontal sampling lines, and is then processed by the same tensor-product procedure. For a mildly rough boundary patch, the smooth-cover correction adds a one-unknown completion on each sampling line before the standard curved-patch solver is applied. These boundary operations are more involved than the rectangular-patch computation, but their sizes are still determined only by the fixed local parameters.

Let N_p be the total number of computational patches. For fixed local resolution, the cost of each local operation is

uniformly bounded, and hence the total online cost is $O(N_p)$. Since $N_p = O(K_x K_y)$ for a fixed Cartesian background partition, and the corresponding global fine-grid sizes satisfy

$$M_x = K_x(m - 1) + 1, \quad M_y = K_y(m - 1) + 1,$$

the total number of retained output points is of order $M_x M_y \sim K_x K_y m^2$. Thus, for fixed local resolution m , the online computational cost is essentially linear in the global number of retained output points.

The memory requirement is also local. The reference SVD factors are stored once, and the patches can be processed independently. No global dense Fourier extension matrix is formed. This locality is one of the main advantages of the proposed method: the geometric complexity of the domain is confined to the patch construction and local boundary transfers, while the algebraic approximation step remains a collection of fixed-size tensor-product LFE computations.

7. Numerical experiments

In this section, we present numerical experiments to illustrate the accuracy and robustness of the proposed patch-wise local Fourier extension method. We first test the method on a smooth curved domain, and then consider a domain whose boundary contains small-scale rough perturbations. Unless otherwise specified, the local Fourier extension parameters are fixed throughout this section.

7.1. Experimental setting

We first consider a curved domain $\Omega \subset [0, 1]^2$ enclosed by the parametric boundary

$$\begin{aligned} x(t) &= 0.50 + 0.38 \cos t + 0.06 \cos(2t + 0.6) - 0.03 \sin(3t), \\ y(t) &= 0.50 + 0.40 \sin t - 0.08 \sin(2t - 0.4) + 0.03 \cos(3t + 0.2), \quad 0 \leq t < 2\pi. \end{aligned} \tag{9}$$

The domain is embedded into a Cartesian background grid with $K_x = K_y = K$. The boundary is scanned once, and the scan is used to generate rectangular interior patches, one-side curved boundary patches of type L, T, R , or B , and additional corner-cover patches near transition regions.

On each patch, $m \times m$ local sampling values are used. The default parameters are

$$T = 4, \quad \gamma_0 = 1.2, \quad n = 10,$$

in both coordinate directions, so that

$$m = \lfloor \gamma_0(2n + 1) \rfloor = 25.$$

The local approximation is evaluated on a refined grid with refinement factor $r = 5$. The truncated singular value decomposition is used with a threshold close to machine precision. When several patches generate the same physical point in the assembled point cloud, the value computed first is retained.

For a given patch P , let

$$\mathcal{G}_P = \{(x_\ell, y_\ell)\}_{\ell=1}^{N_P}$$

be the refined physical evaluation grid associated with this patch, and let f_h denote the local patchwise approximation. We define the patchwise maximum error by

$$E_\infty(P) = \max_{1 \leq \ell \leq N_P} |f_h(x_\ell, y_\ell) - f(x_\ell, y_\ell)|.$$

For each patch type, the reported E_∞^{\max} is the maximum of $E_\infty(P)$ over all patches of that type, while

$$E_\infty^{\text{avg}} = \frac{1}{\#\mathcal{P}_{\text{type}}} \sum_{P \in \mathcal{P}_{\text{type}}} E_\infty(P)$$

denotes the average of the patchwise maximum errors over all patches of that type. For curved boundary patches, the refined grid follows the corresponding curved side, so that the numerical approximation and the exact function are compared on the same physical patch.

7.2. Influence of the background partition on a smooth curved domain

We first examine the influence of the background partition on the smooth curved domain (9). The test function is

$$f(x, y) = \frac{\sin(xy)}{1 + y^2}.$$

This function is smooth and of low frequency on the computational domain, so the test mainly reflects the effect of the curved boundary patches and the scan-based partition.

Figure 7 shows the result for $K_x = K_y = 20$. The left panel gives the exact function, the middle panel shows the assembled patchwise approximation, and the right panel displays the pointwise error on a logarithmic scale. The maximum pointwise error is about 5.795×10^{-12} .

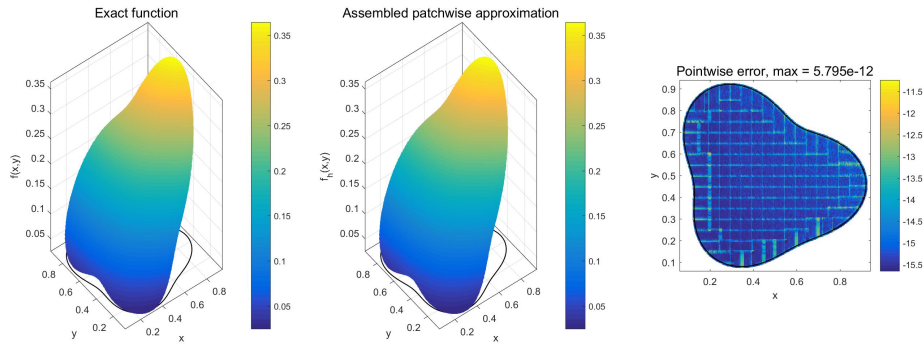


Figure 7: Approximation of $f(x, y) = \sin(xy)/(1 + y^2)$ on the smooth curved domain with $K_x = K_y = 20$. Left: exact function. Middle: assembled patchwise approximation. Right: pointwise error in logarithmic scale.

Table 3 reports the patchwise maximum errors and their averages for different background partitions. The number of patches is also listed, since for fixed local parameters it is the main indicator of the online cost.

The table shows that the rectangular patches already reach very high accuracy for moderate partitions. For coarse partitions, the larger errors are mainly associated with curved boundary patches, where a single patch may contain a relatively long portion of the boundary. As the partition is refined, the boundary portion represented by each patch becomes shorter and the normalized geometric deformation is reduced. For $K_x = K_y = 20$, all patch types reach an accuracy close to 10^{-12} or better. In the following experiments we therefore use $K_x = K_y = 20$ as the default background partition.

Table 3: Errors for different background partitions for $f(x, y) = \sin(xy)/(1 + y^2)$ on the smooth curved domain.

$K_x = K_y$	number of patches	rect		left		right		top		bottom	
		E_∞^{\max}	E_∞^{avg}	E_∞^{\max}	E_∞^{avg}	E_∞^{\max}	E_∞^{avg}	E_∞^{\max}	E_∞^{avg}	E_∞^{\max}	E_∞^{avg}
5	14	–	–	3.91e-11	1.72e-11	2.81e-07	9.38e-08	1.42e-08	4.20e-09	6.48e-12	4.80e-12
10	40	4.66e-13	2.04e-13	1.07e-09	1.36e-10	2.90e-12	2.59e-12	8.84e-10	1.27e-10	2.70e-12	1.42e-12
15	92	7.40e-13	1.96e-13	2.28e-12	1.35e-12	3.05e-12	2.32e-12	4.29e-12	2.06e-12	2.92e-12	1.90e-12
20	170	7.83e-13	1.91e-13	7.99e-13	3.95e-13	5.79e-12	3.16e-12	4.19e-12	1.59e-12	1.43e-12	7.08e-13

7.3. Full-domain test with a mildly rough boundary

We next test the method on a domain whose boundary contains small-scale local perturbations. To make the experiment reproducible, we explicitly describe the construction of the perturbed boundary. We start from the smooth closed reference curve

$$\rho_0(t) = 1 + 0.18 \cos(3t) - 0.08 \sin(2t),$$

$$X_0(t) = \rho_0(t) \cos t, \quad Y_0(t) = 0.82\rho_0(t) \sin t.$$

After affine rescaling of (X_0, Y_0) into the box $[0.08, 0.92]^2$, we obtain a smooth curve $(x_0(t), y_0(t))$. The mildly rough boundary is then defined by a small radial perturbation with respect to the center $(0.5, 0.5)$:

$$x_r(t) = 0.5 + (1 + \rho_1(t))(x_0(t) - 0.5), \quad y_r(t) = 0.5 + (1 + \rho_1(t))(y_0(t) - 0.5),$$

where

$$\begin{aligned} \rho_1(t) = & 0.012 \operatorname{sgn}(\sin(12t + 0.40)) |\sin(12t + 0.40)|^{1.20} \\ & + 0.007 \operatorname{sgn}(\cos(17t - 0.20)) |\cos(17t - 0.20)|^{1.20} + 0.003 \sin(25t + 0.80). \end{aligned}$$

This construction preserves the overall shape of the smooth reference curve, while introducing visible small-scale perturbations along the boundary.

The scan-based partition for this domain is shown in Figure 6. The same patch classification is used as in the smooth case, while the smooth-cover correction described in Section 5.3 is applied to the boundary patches of type L , T , R , and B .

We first use the same test function

$$f(x, y) = \frac{\sin(xy)}{1 + y^2}.$$

Table 4 reports the patchwise errors for different background partitions.

Table 4: Errors for different background partitions for $f(x, y) = \sin(xy)/(1 + y^2)$ on a mildly rough boundary domain.

$K_x = K_y$	number of patches	rect		left		right		top		bottom	
		E_∞^{\max}	E_∞^{avg}	E_∞^{\max}	E_∞^{avg}	E_∞^{\max}	E_∞^{avg}	E_∞^{\max}	E_∞^{avg}	E_∞^{\max}	E_∞^{avg}
5	14	–	–	5.34e-11	4.56e-11	7.34e-12	3.46e-12	2.50e-11	6.57e-12	1.90e-10	1.05e-10
10	40	4.66e-13	2.04e-13	4.06e-11	1.48e-11	6.58e-12	4.09e-12	2.11e-12	1.13e-12	2.02e-10	7.64e-11
15	93	7.40e-13	1.99e-13	2.27e-10	5.30e-11	4.06e-12	2.60e-12	6.69e-12	1.89e-12	1.03e-10	3.37e-11
20	173	7.83e-13	1.90e-13	4.64e-12	1.34e-12	2.66e-10	7.44e-11	5.31e-11	2.08e-11	3.49e-12	2.04e-12

With the smooth-cover correction, the boundary patch errors remain stable despite the small-scale perturbations of the boundary. Compared with a direct treatment of the perturbed boundary, the cover correction reduces the sensitivity of boundary patches to local geometric oscillations. At the same time, the partition size still affects the overall approximation through the local frequency reduction discussed in Remark 3.2. We therefore keep $K_x = K_y = 20$ in the remaining tests on the rough boundary domain.

Figure 8 compares the results obtained without and with the smooth-cover correction for $K_x = K_y = 20$. Without the cover correction, the maximum pointwise error is about 3.609×10^{-5} , and the larger errors are concentrated near boundary patches. After applying the local smooth-cover correction, the maximum pointwise error is reduced to about 1.298×10^{-10} .

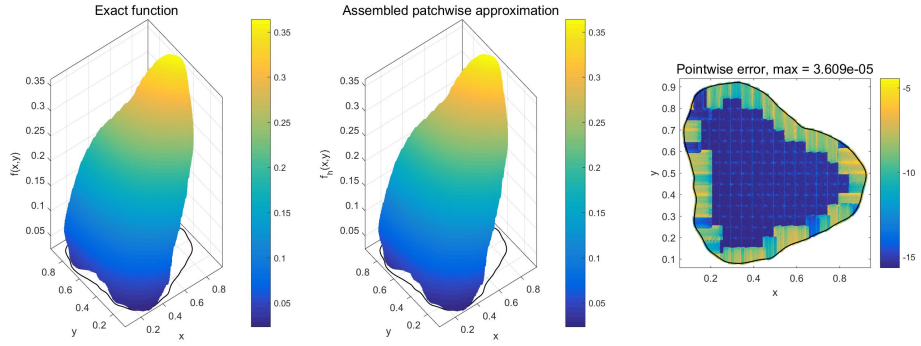
Finally, we test the same rough boundary domain and the same cover-corrected setting on four additional functions:

$$f_1(x, y) = \text{erf}(20(x - y)), \quad f_2(x, y) = \frac{\log(10(x + y))}{\sqrt{x^2 + y}},$$

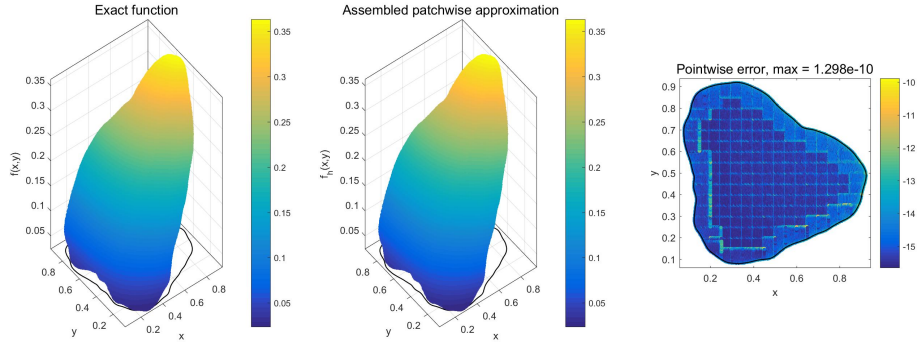
$$f_3(x, y) = \sin(20(x^2 + y^2)), \quad f_4(x, y) = \text{Ai}(-15 - 13(x + y)),$$

where Ai denotes the Airy function. Figure 9 shows the corresponding results. The maximum pointwise errors are approximately 1.447×10^{-9} , 4.445×10^{-9} , 1.099×10^{-9} , 1.618×10^{-10} , respectively. These tests show that the same cover-corrected patchwise framework remains accurate for functions with different local behaviors on the mildly rough boundary domain.

The error plots also show that the relatively larger errors often appear near patch interfaces or near boundary-related subregions. This is expected for a non-overlapping patchwise assembly. A possible further improvement is to use overlapping patches and retain only the central or better-conditioned part of each local approximation. Such an overlap-and-restriction strategy may reduce interface effects, but we leave this refinement for future work.

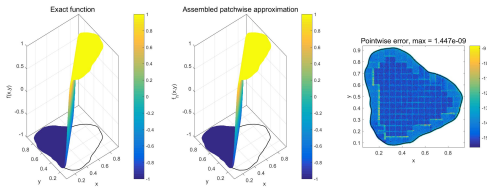


(a) Direct treatment of the mildly rough boundary without the smooth-cover correction. The maximum pointwise error is 3.609×10^{-5} .

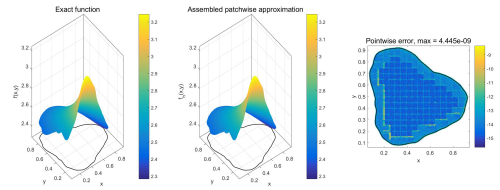


(b) Result obtained with the smooth-cover correction applied to boundary patches. The maximum pointwise error is reduced to 1.298×10^{-10} .

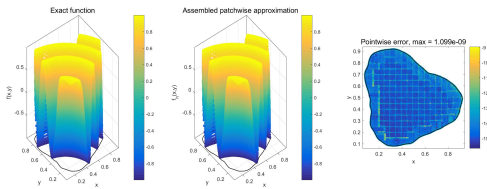
Figure 8: Effect of the smooth-cover correction on the mildly rough boundary domain for $f(x, y) = \sin(xy)/(1 + y^2)$ with $K_x = K_y = 20$.



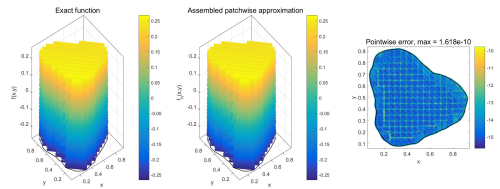
(a) $f_1(x, y) = \text{erf}(20(x - y))$, max error = 1.447×10^{-9} .



(b) $f_2(x, y) = \log(10(x + y))/\sqrt{x^2 + y}$, max error = 4.445×10^{-9} .



(c) $f_3(x, y) = \sin(20(x^2 + y^2))$, max error = 1.099×10^{-9} .



(d) $f_4(x, y) = \text{Ai}(-15 - 13(x + y))$, max error = 1.618×10^{-10} .

Figure 9: Pointwise error plots for four additional test functions on the mildly rough boundary domain with $K_x = K_y = 20$.

7.4. A brief timing test

To further illustrate the computational behavior of the proposed method, we also report a simple timing test for the mildly rough boundary case. In this experiment, we remove auxiliary post-processing steps such as refined-grid evaluation and visualization, and only retain the essential geometric preprocessing and patchwise approximation steps. Figure 10 reports the timing results. Since the local parameters are fixed, the number of retained output points

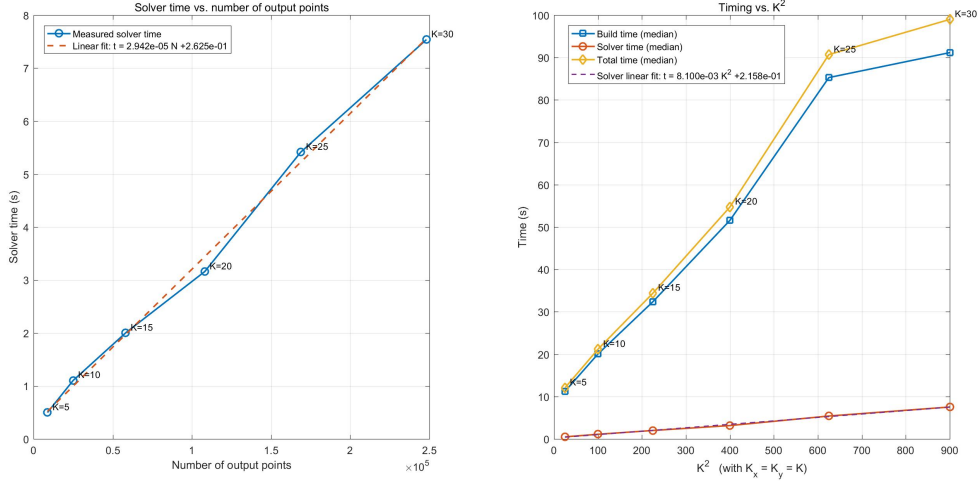


Figure 10: Timing test for the patchwise solver on the mildly rough boundary domain. The left panel shows solver time versus the number of retained output points, and the right panel separates the build, solver, and total times versus K^2 .

is proportional to $K_x K_y$; in the present tests $K_x = K_y = K$, so the expected linear online complexity corresponds to a nearly linear dependence on K^2 . The left panel confirms that the solver time grows approximately linearly with the number of retained output points. The right panel separates the build, solver, and total times. The build stage is more expensive in this implementation because it includes the geometric preprocessing, especially the computation of intersections between the boundary curve and Cartesian grid lines. This preprocessing is performed only once for a fixed domain and can be reused when approximating different functions on the same geometry.

8. Conclusions and remarks

We have presented a patchwise local Fourier extension method for function approximation on two-dimensional domains with curved boundaries. The method embeds the physical domain into a Cartesian background grid and decomposes it into rectangular interior patches and one-side curved boundary patches. After local data transfer, each patch is represented by a fixed-size tensor-product array and approximated by a TSVD-stabilized local Fourier extension procedure. This construction avoids forming a single global Fourier frame system and localizes both the geometric treatment and the ill-conditioned extension step.

For fixed local parameters, the local algebraic systems have bounded size and the reference one-dimensional SVDs can be precomputed and reused. Boundary patches require additional line transfers, and mildly rough boundary patches also require a one-unknown completion on each sampling line, but these steps remain local. The timing test confirms that, after the geometric preprocessing stage, the online solver time grows approximately linearly with the number of retained output points. The build stage is more dependent on the boundary representation, since in the current implementation its main cost is the computation of boundary–grid intersections.

The numerical experiments show that the method achieves high accuracy on smooth curved domains with a fixed set of parameters. They also demonstrate that the smooth-cover correction can substantially reduce boundary-induced errors for mildly rough boundary patches without changing the scan-based partition logic. The larger errors observed in some tests are mainly located near patch interfaces or boundary-related subregions, which is consistent with the non-overlapping assembly used in the present implementation.

Several extensions are natural. Adaptive refinement could be used to refine only patches with large local frequency, geometric distortion, or cover-correction residuals. An overlap-and-restriction assembly may further reduce interface effects by retaining only the central or better-conditioned part of each local approximation. A systematic treatment of more general nonsmooth domains would require automatic boundary segmentation, robust cover construction, and a stability analysis of the artificial boundary completion. Finally, the patchwise LFE representation is a promising ingredient for high-order PDE solvers on curved domains, either through alternating-direction or domain-decomposition strategies based on one-dimensional LFE operators, or through point-driven local collocation schemes.

Acknowledgments

The research is partially supported by National Natural Science Foundation of China (Nos. 42450232, 12171455).

References

- [1] Y. Wang, I. Stepanova, V. Titarenko, A. Yagola, *Inverse Problems in Geophysics and Solution Methods.*, Higher Education Press, 2011.
- [2] J. P. Boyd, A comparison of numerical algorithms for Fourier extension of the first, second, and third kinds, *Journal of Computational Physics* 178 (1) (2002) 118–160.
- [3] J. P. Boyd, Fourier embedded domain methods: Extending a function defined on an irregular region to a rectangle so that the extension is spatially periodic and smooth, *Applied Mathematics and Computation* 161 (2) (2005) 591–597.
- [4] O. P. Bruno, Y. Han, M. M. Pohlman, Accurate, high-order representation of complex three-dimensional surfaces via Fourier continuation analysis, *Journal of Computational Physics* 227 (2) (2007) 1094–1125.

- [5] O. P. Bruno, M. Lyon, High-order unconditionally stable FC-AD solvers for general smooth domains I. basic elements, *Journal of Computational Physics* 229 (6) (2010) 2009–2033.
- [6] M. Lyon, O. P. Bruno, High-order unconditionally stable FC-AD solvers for general smooth domains II. elliptic, parabolic and hyperbolic PDEs; theoretical considerations, *Journal of Computational Physics* 229 (9) (2010) 3358–3381.
- [7] R. Matthysen, D. Huybrechs, Function approximation on arbitrary domains using Fourier extension frames, *SIAM Journal on Numerical Analysis* 56 (3) (2018) 1360–1385.
- [8] B. Adcock, D. Huybrechs, Approximating smooth, multivariate functions on irregular domains 8 (2020) e26.
- [9] D. Huybrechs, On the Fourier extension of nonperiodic functions, *SIAM Journal on Numerical Analysis* 47 (6) (2010) 4326–4355.
- [10] B. Adcock, D. Huybrechs, J. Martín-Vaquero, On the numerical stability of Fourier extensions, *Foundations of Computational Mathematics* 14 (2014) 635–687.
- [11] B. Adcock, D. Huybrechs, On the resolution power of Fourier extensions for oscillatory functions, *Journal of computational and applied mathematics* 260 (2014) 312–336.
- [12] B. Adcock, D. Huybrechs, Frames and numerical approximation, *SIAM Review* 61 (3) (2019) 443–473.
- [13] N. Albin, O. P. Bruno, A spectral FC solver for the compressible Navier–Stokes equations in general domains I: Explicit time-stepping, *Journal of Computational Physics* 230 (16) (2011) 6248–6270.
- [14] O. P. Bruno, J. Paul, Two-dimensional Fourier continuation and applications, *SIAM Journal on Scientific Computing* 44 (2) (2022) A964–A992.
- [15] Z. Zhao, Y. Wang, A local Fourier extension method for function approximation, *Inverse Problems and Imaging* 22 (2026) 1–13.